Application of the Semi-Lagrangian Method to a Spectral Model of the Shallow Water Equations

HAROLD RITCHIE

Recherche en Prévision Numérique, Atmospheric Environment Service, Dorval, Québec, Canada

(Manuscript received 14 September 1987, in final form 22 January 1988)

ABSTRACT

Previous tests with grid-point numerical weather prediction models have shown that semi-Lagrangian schemes permit the use of time steps that are much larger than those permitted by the Courant–Friedrichs–Lewy (CFL) stability criterion for the corresponding Eulerian models, without reducing the accuracy of the forecasts. Thus model efficiency is improved because fewer time steps are needed to complete the forecast.

In a first step to see if similar results can be achieved in spectral models, Ritchie, in a previous study, applied interpolating and noninterpolating semi-Lagrangian treatments of advection to the problem of simple advection by a steady wind field on a Gaussian grid. This present paper combines these treatments of advection with the semi-implicit scheme in a spectral model of the shallow water equations expressed in vector momentum form. Model formulations are presented and intercomparison experiments are performed. It is shown that both interpolating and noninterpolating semi-Lagrangian schemes can be applied accurately and stably to a spectral model of the shallow water equations with time steps that are much larger than the CFL limit for the corresponding Eulerian model.

1. Introduction

Largely because of its very attractive stability properties, the semi-Lagrangian time integration scheme is being used in numerical weather prediction models in combination with an increasing number of spatial discretizations. Numerous investigators have tested it in grid point models and have shown that it permits the use of time steps that are much larger than those permitted by the Courant–Friedrichs–Lewy (CFL) stability criterion for the corresponding Eulerian models. This leads to improved model efficiency, since fewer steps are needed to complete the forecasts. In a study of the barotropic vorticity equation, Sawyer (1963) showed that this approach is unconditionally stable for Rossby waves and gives an accuracy comparable to that of Eulerian methods. By virtue of the stability of the semi-implicit scheme for the treatment of gravity waves, Robert (1981, 1982) succeeded in combining the semi-implicit scheme with the semi-Lagrangian scheme to produce stable and accurate integrations of grid point models of the shallow water equations using large time steps. Applications of the semi-Lagrangian scheme to multilevel primitive equations grid point models have been presented by Bates and McDonald (1982) in combination with a split explicit scheme, by Robert et al. (1985) in conjunction with the semi-implicit method, and by McDonald (1986) in an unconditionally stable two time level integration scheme.

There have also been several applications in the context of the regional finite element model developed at Recherche en prévision numérique (RPN). Ritchie (1985) took advantage of this method's accurate phase characteristics and used it in treating the moisture equation in the multilevel regional model. Staniforth and Temperton (1986) applied a three time level semi-implicit semi-Lagrangian scheme to a shallow water equations version of the model, and more recently Temperton and Staniforth (1987) tested a two time level version of this model.

In preparation for applying the semi-Lagrangian method to spectral models, Ritchie (1987) studied the problem of simple advection by a steady wind field on a Gaussian grid. The geometric and linear stability aspects of interpolating and noninterpolating (see Ritchie 1986) semi-Lagrangian treatments of advection on a Gaussian grid were examined. The objective of this present investigation is to combine these treatments of advection with the semi-implicit scheme in a spectral model of the shallow water equations. A conventional vorticity–divergence Eulerian formulation is presented in section 2, where an equivalent Eulerian momentum equation formulation is also developed in order to facilitate the introduction of the semi-Lagrangian method. Interpolating and noninterpolating semi-Lagrangian versions of the latter formulation (in vector

Corresponding author address: Harold Ritchie, Recherche en Prévision Numérique, 2121 Trans-Canada Highway, Suite 508, Dorval, Québec, Canada H9P 1J3.

form) are presented in section 3. Model intercomparison experiments in section 4 confirm the equivalence of the Eulerian models formulated in section 2 and assess the impact of the semi-Lagrangian treatments presented in section 3. The Appendix examines the transformation of horizontal vectors to the tangential Cartesian plane, as used for the discretization of the semi-Lagrangian models in section 3.

2. Eulerian model formulations

a. *Vorticity–divergence form*

Since most of the spectral models used in numerical weather prediction express the horizontal motion in terms of the vorticity equation and the divergence equation, a conventional vorticity–divergence (ζ–D) formulation was chosen as the starting point for this intercomparison of spectral models of the shallow water equations. This version was produced by reducing the RPN multilevel model (for a basic description, see Daley et al. 1976) to a single level, resulting in a model that is similar in many respects to those used by other researchers (e.g., Bourke 1972). An outline of this formulation is presented here for the purpose of emphasizing similarities and differences with other formulations in subsequent sections.

The vorticity, divergence, and continuity equations can be written, respectively, as

$$\frac{\partial \zeta}{\partial t} = -\alpha(A, B)$$

$$\frac{\partial D}{\partial t} + \overline{\nabla_H{}^2\Phi}^{t} = \alpha(B, -A) - a^2\nabla_H{}^2E$$

$$\frac{\partial \Phi}{\partial t} + \Phi^*\bar{D}^{t} = -\alpha(U\Phi, V\Phi)$$

where

$$\mathbf{v}_H = u\hat{\lambda} + v\hat{\theta} = \nabla_H\chi + \mathbf{k}\times\nabla_H\psi$$

$$\alpha(A, B) = \frac{1}{\cos^2\theta}\left\{\frac{\partial A}{\partial\lambda} + \cos\theta\,\frac{\partial B}{\partial\theta}\right\}$$

$$A = (\zeta + 2\Omega\sin\theta)U$$

$$B = (\zeta + 2\Omega\sin\theta)V$$

$$U = \frac{u\cos\theta}{a} = \frac{1}{a^2}\frac{\partial\chi}{\partial\lambda} - \frac{\cos\theta}{a^2}\frac{\partial\psi}{\partial\theta} \tag{1}$$

$$V = \frac{v\cos\theta}{a} = \frac{1}{a^2}\frac{\partial\psi}{\partial\lambda} + \frac{\cos\theta}{a^2}\frac{\partial\chi}{\partial\theta} \tag{2}$$

$$\zeta = \alpha(V, -U) = \nabla_H{}^2\psi \tag{3}$$

$$D = \alpha(U, V) = \nabla_H{}^2\chi \tag{4}$$

$$E = \frac{U^2 + V^2}{2\cos^2\theta}$$

and

$$\nabla_H{}^2G = \frac{1}{a^2\cos^2\theta}\left\{\frac{\partial^2 G}{\partial\lambda^2} + \cos\theta\,\frac{\partial}{\partial\theta}\left(\cos\theta\,\frac{\partial G}{\partial\theta}\right)\right\}.$$

These equations describe the motion of a hydrostatic, homogeneous, incompressible fluid on a rotating sphere. Here λ is longitude and θ latitude in a spherical polar coordinate system with unit vectors $\hat{\lambda}$, $\hat{\theta}$ and $\mathbf{k}$ in the eastward, northward, and vertical directions, respectively; $\mathbf{v}_H$ is the horizontal velocity, ζ the vorticity, D the divergence, ψ the streamfunction, χ the velocity potential function, Φ the perturbation geopotential of the free upper surface of the fluid, Φ^* a constant roughly equal to the mean geopotential, Ω the earth's angular rotation rate, and a the earth's radius.

In a centered scheme the time derivatives are approximated by

$$\frac{\partial F}{\partial t} \approx \frac{F(\lambda, \theta, t + \Delta t) - F(\lambda, \theta, t - \Delta t)}{2\Delta t} \tag{5}$$

where Δt is the time step increment. For a semi-implicit treatment of the terms that produce gravity waves, the time averaging operator is prescribed by

$$\bar{F}^{t} = \frac{1}{2}\{F(\lambda, \theta, t + \Delta t) + F(\lambda, \theta, t - \Delta t)\}. \tag{6}$$

Suppressing reference to (λ, θ), the time discretized equations become

$$\zeta|_{t+\Delta t} = \zeta|_{t-\Delta t} - 2\Delta t\alpha(A, B)|_t \equiv L \tag{7}$$

$$(D + \Delta t\nabla_H{}^2\Phi)|_{t+\Delta t} = (D - \Delta t\nabla_H{}^2\Phi)|_{t-\Delta t} - 2\Delta t\{a^2\nabla_H{}^2E - \alpha(B, -A)\}|_t \equiv M \tag{8}$$

$$(\Phi + \Delta t\Phi^*D)|_{t+\Delta t} = (\Phi - \Delta t\Phi^*D)|_{t-\Delta t} - 2\Delta t\alpha(U\Phi, V\Phi)|_t \equiv Q. \tag{9}$$

Eliminating $D(\lambda, \theta, t + \Delta t)$ from Eqs. (8) and (9) leads to the following Helmholtz equation to solve for $\Phi(\lambda, \theta, t + \Delta t)$:

$$\Phi - \Delta t^2\Phi^*\nabla_H{}^2\Phi = Q - \Delta t\Phi^*M. \tag{10}$$

Thus, knowing L, M and Q, we can solve (7) for $\zeta(\lambda, \theta, t + \Delta t)$, (10) for $\Phi(\lambda, \theta, t + \Delta t)$ and then (8) for $D(\lambda, \theta, t + \Delta t)$. To solve this system in spectral space, making substitutions of the form

$$F(\lambda, \theta, t) = \sum_m \sum_n F_n^m(t)Y_n^m(\lambda, \theta)$$

for ζ, D, Φ, L, M and Q, and using the following result valid for spherical harmonics $Y_n^m(\lambda, \theta)$

$$\nabla_H{}^2\{F_n^mY_n^m(\lambda, \theta)\} = \frac{-n(n+1)}{a^2}F_n^mY_n^m(\lambda, \theta) \tag{11}$$

produces the following equations for the forecast spectral coefficients

$$\zeta_n^m(t + \Delta t) = L_n^m$$

$$\Phi_n^m(t + \Delta t) = \left\{1 + \Delta t^2 \Phi^* \frac{n(n+1)}{a^2}\right\}^{-1} \{Q_n^m - \Delta t \Phi^* M_n^m\}$$

$$D_n^m(t + \Delta t) = \Delta t \frac{n(n+1)}{a^2} \Phi_n^m + M_n^m.$$

Having found $\zeta_n^m(t + \Delta t)$, $D_n^m(t + \Delta t)$, $\Phi_n^m(t + \Delta t)$ in spectral space, inverse transforms are performed to find $\zeta(\lambda, \theta, t + \Delta t)$, $D(\lambda, \theta, t + \Delta t)$, $\Phi(\lambda, \theta, t + \Delta t)$, and (11), (3), (4), (1) and (2) are also used to find $U(\lambda, \theta, t + \Delta t)$ and $V(\lambda, \theta, t + \Delta t)$ on the Gaussian (λ, θ) grid, thus completing the time step.

b. *Momentum form*

Since Lagrangian derivatives arise more naturally in the momentum (U–V) form of the horizontal equations of motion than they do in the ζ–D equations, U–V formulations are more appropriate for semi-Lagrangian models. In preparation for applying the semi-Lagrangian scheme, this subsection presents an Eulerian spectral U–V model which does not use an explicit spectral representation of U and V, and shows that the resulting model is algebraically equivalent to the ζ–D one presented in the previous subsection. For examples of U–V models using spectral representations of the wind images U and V, see Robert 1966, Eliasen et al. 1970, and the summary by Machenhauer 1979.

When expressed in terms of U and V, the vector form of the horizontal momentum equation

$$\frac{\partial \mathbf{v}_H}{\partial t} + (\mathbf{v}_H \cdot \nabla_H)\mathbf{v}_H + f\mathbf{k} \times \mathbf{v}_H + \nabla_H \Phi = \mathbf{0} \quad (12)$$

leads to

$$\frac{\partial U}{\partial t} + \frac{1}{a^2} \overline{\frac{\partial \Phi}{\partial \lambda}}^t = -\{A(U, V, U) - fV\} \quad (13)$$

$$\frac{\partial V}{\partial t} + \frac{\cos\theta}{a^2} \overline{\frac{\partial \Phi}{\partial \theta}}^t = -\{A(U, V, V) + fU + 2\sin\theta E\} \quad (14)$$

where $f = 2\Omega \sin\theta$ is the Coriolis parameter and

$$A(U, V, F) = \frac{1}{\cos^2\theta}\left\{U\frac{\partial F}{\partial \lambda} + V\cos\theta \frac{\partial F}{\partial \theta}\right\}.$$

The continuity equation can be expressed as

$$\frac{\partial \Phi}{\partial t} + \Phi^* \bar{D}^t = -\{A(U, V, \Phi) + \Phi D\}. \quad (15)$$

Using the same time discretization (5) and (6) as before yields

$$\left(U + \frac{\Delta t}{a^2}\frac{\partial \Phi}{\partial \lambda}\right)\Big|_{t+\Delta t} = P_1|_{t-\Delta t} - 2\Delta t R_1|_t \equiv Q_1 \quad (16)$$

$$\left(V + \frac{\Delta t}{a^2}\cos\theta \frac{\partial \Phi}{\partial \theta}\right)\Big|_{t+\Delta t} = P_2|_{t-\Delta t} - 2\Delta t R_2|_t \equiv Q_2 \quad (17)$$

$$(\Phi + \Delta t \Phi^* D)|_{t+\Delta t} = P_3|_{t-\Delta t} - 2\Delta t R_3|_t \equiv Q_3 \quad (18)$$

where

$$P_1 = U - \frac{\Delta t}{a^2}\frac{\partial \Phi}{\partial \lambda} \quad (19)$$

$$P_2 = V - \frac{\Delta t}{a^2}\cos\theta \frac{\partial \Phi}{\partial \theta} \quad (20)$$

$$P_3 = \Phi - \Delta t \Phi^* D \quad (21)$$

$$R_1 = A(U, V, U) - fV \quad (22)$$

$$R_2 = A(U, V, V) + fU + 2\sin\theta E \quad (23)$$

$$R_3 = A(U, V, \Phi) + \Phi D. \quad (24)$$

Evaluating $A(U, V, U)$ and $A(U, V, V)$ requires $\partial U/\partial\lambda$, $\cos\theta \partial U/\partial\theta$, $\partial V/\partial\lambda$ and $\cos\theta \partial V/\partial\theta$. Having values of U and V on the Gaussian grid, grid point values of $\partial U/\partial\lambda$ and $\partial V/\partial\lambda$ are calculated using fast Fourier transforms (note that this does not require Legendre transforms or explicit spectral representations of U and V). On the Gaussian grid these results can be combined with values of ζ and D to calculate

$$\cos\theta \frac{\partial U}{\partial \theta} = \frac{\partial V}{\partial \lambda} - \zeta \cos^2\theta$$

$$\cos\theta \frac{\partial V}{\partial \theta} = D\cos^2\theta - \frac{\partial U}{\partial \lambda}.$$

To solve (16)–(18), we cross differentiate (16) and (17) to calculate

$$\zeta|_{t+\Delta t} = \alpha(Q_2, -Q_1) \equiv L^* \quad (25)$$

$$(D + \Delta t \nabla_H{}^2 \Phi)|_{t+\Delta t} = \alpha(Q_1, Q_2) \equiv M^* \quad (26)$$

and eliminate with $D|_{t+\Delta t}$ in (18) to get

$$\Phi - \Delta t^2 \Phi^* \nabla_H{}^2 \Phi = Q_3 - \Delta t \Phi^* M^*. \quad (27)$$

The system of equations (25)–(27) is identical in form to the corresponding system (7), (8), and (10) for the ζ–D model, so it is solved spectrally and the time step is completed in exactly the same way as in the ζ–D model.

The algebraic equivalence of the ζ–D and U–V Eulerian models is established as follows. The identity

$$\alpha(U\Phi, V\Phi) = A(U, V, \Phi) + \Phi D$$

gives $Q_3 = Q$. The terms evaluated at $t - \Delta t$ in L^* and L agree, since $\alpha(P_2, -P_1) = \zeta$. From the fact that

$$\frac{\partial}{\partial\lambda}\{A(U, V, V) + 2\sin\theta E\} - \cos\theta\frac{\partial}{\partial\theta}\{A(U, V, U)\}$$
$$= \frac{\partial}{\partial\lambda}(\zeta U) + \cos\theta\frac{\partial}{\partial\theta}(\zeta V)$$

it follows that $\alpha(R_2, -R_1) = \alpha(A, B)$. Hence the terms evaluated at t in L^* and L agree, so that $L^* = L$. Similarly, the terms evaluated at $t - \Delta t$ in M^* and M are equal since

$$\alpha(P_1, P_2) = D - \Delta t\nabla_H{}^2\Phi.$$

It can also be shown that

$$\alpha(R_1, R_2) = a^2\nabla_H{}^2E - \alpha(B, -A)$$

so the terms evaluated at t in M^* and M are equal, and the U–V and ζ–D Eulerian models are algebraically equivalent. This simply emphasizes that the terms evaluated at time t can be expressed in advective form rather than flux form, and that the time discretized vorticity and divergence equations can be found by cross differentiating the time discretized momentum equations.

3. Semi-Lagrangian model formulations

Probably the most apparent way to transform the Eulerian U–V spectral model of the shallow water equations into a semi-Lagrangian one is to start with the scalar equations (13), (14) and (15) which control the evolution of U, V and Φ respectively, and treat the total derivative of each scalar

$$\frac{dF}{dt} = \frac{\partial F}{\partial t} + A(U, V, F)$$

with a semi-Lagrangian discretization as done by Ritchie (1987). This approach was attempted and works well for the continuity equation (15), but for equation (14) it was found that an unexpected problem developed near the poles $\theta = \pm\pi/2$ due to an instability associated with the metric term $2\sin\theta E$ when a semi-Lagrangian treatment is used for the advection of V. For this reason it was decided to do a vector discretization of the vector form of the horizontal momentum equation (12), and thus avoid an explicit treatment of the metric term. In this section the resulting time discretization is presented in a general form from which Eulerian, interpolating semi-Lagrangian, and noninterpolating semi-Lagrangian versions are recovered.

Breaking $\mathbf{v}_H$ into two parts

$$\mathbf{v}_H = \mathbf{v}_H^* + \mathbf{v}'_H$$

in the horizontal advection operator $\mathbf{v}_H\cdot\nabla_H$, the vector horizontal momentum equation (12) can be written as

$$\frac{\partial\mathbf{v}_H}{\partial t} + (\mathbf{v}_H^*\cdot\nabla_H)\mathbf{v}_H + \overline{\nabla_H\Phi}^t$$
$$= -\{(\mathbf{v}'_H\cdot\nabla_H)\mathbf{v}_H + f\mathbf{k}\times\mathbf{v}_H\} \quad (28)$$

and the continuity equation (15) becomes

$$\frac{\partial\Phi}{\partial t} + \mathbf{v}_H^*\cdot\nabla_H\Phi + \Phi^*\bar{D}^t = -(\mathbf{v}'_H\cdot\nabla_H\Phi + \Phi D), \quad (29)$$

where the operator

$$\frac{\partial}{\partial t} + \mathbf{v}_H^*\cdot\nabla_H$$

gives the total derivative following a point that moves with velocity $\mathbf{v}_H^*$. In this way, $\mathbf{v}_H^*$ represents the portion of the advecting velocity that is treated with a semi-Lagrangian approach, while $\mathbf{v}'_H\cdot\nabla_H$ represents the residual advection operator associated with the residual velocity $\mathbf{v}'_H$ and is treated in an Eulerian fashion.

Let $(\ )^+$ denote evaluation at a Gaussian grid point $\mathbf{g}$ at forecast time $t + \Delta t$, $(\ )^-$ denote evaluation at the upstream position at time $t - \Delta t$, and $(\ )^0$ denote evaluation at time t at the midpoint of the intervening trajectory. To apply the centered semi-Lagrangian semi-implicit discretization, the Lagrangian time derivative is approximated by the difference along the trajectory

$$\frac{\partial}{\partial t} + \mathbf{v}_H^*\cdot\nabla_H \approx \frac{(\ )^+ - (\ )^-}{2\Delta t}$$

while the time average is approximated by the average along the trajectory

$$\overline{(\ )}^t \approx \frac{1}{2}\{(\ )^+ + (\ )^-\}.$$

With this time discretization, the continuity equation (29) becomes

$$(\Phi + \Delta t\Phi^*D)^+ = (P_3)^- - 2\Delta t(r_3)^0 \quad (30)$$

where

$$(r_3)^0 = \{A(U, V, \Phi) + \Phi D\}^0$$
$$- \frac{u^*}{a}\left(\frac{1}{\cos\theta}\frac{\partial\Phi}{\partial\lambda}\right)^0 - \frac{v^*}{a}\left(\frac{\partial\Phi}{\partial\theta}\right)^0 \quad (31)$$

with P_3 as given by (21) and

$$\mathbf{v}_H^* = u^*\hat{\lambda} + v^*\hat{\theta}.$$

Since $\partial\mathbf{v}_H/\partial t + (\mathbf{v}_H^*\cdot\nabla_H)\mathbf{v}_H$ is the horizontal part of the total derivative of $\mathbf{v}_H$ following a point that moves with velocity $\mathbf{v}_H^*$, it is the derivative as evaluated in a tangential Cartesian coordinate system. This motivates integrating the horizontal momentum equation (28) in tangential Cartesian coordinates. In order to find the transformation to the tangential Cartesian plane for horizontal vectors on a trajectory, we let $\mathbf{c}$ be a unit vector along $\mathbf{v}_H^*$ and let $\mathbf{n}$ be a horizontal unit vector normal and to the left of $\mathbf{c}$. As illustrated in Fig. 1, let α be the angular displacement (positive in the direction

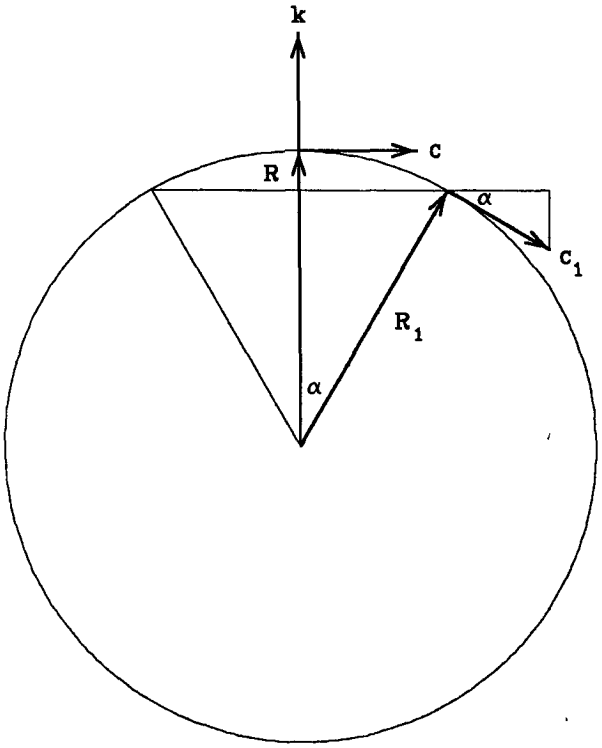

FIG. 1. Schematic diagram of vectors along a trajectory. The reader's perspective lies in a point normal to the plane slicing through the great circle trajectory. **R** represents the position at time t, and $\mathbf{R}_1$ represents the position at time $t + \Delta t$ or at time $t - \Delta t$ as discussed in section 3.

of **c**) along a great circle trajectory between two positions **R** and $\mathbf{R}_1$. We choose **R** to be the position at time t and use the corresponding $\hat{\lambda}^0$ and $\hat{\theta}^0$ as the unit vectors of the tangential Cartesian plane. For a horizontal vector

$$\mathbf{h}_1 = h_\lambda \hat{\lambda}_1 + h_\theta \hat{\theta}_1$$

at position $\mathbf{R}_1$, transforming to the tangential Cartesian plane consists of finding the vector in the $(\hat{\lambda}^0, \hat{\theta}^0)$ plane having the same magnitude as $\mathbf{h}_1$, and whose direction is the projection of $\mathbf{h}_1$ in this plane. This is done by first expressing $\hat{\lambda}_1$ and $\hat{\theta}_1$ in terms of $\mathbf{c}_1$ and $\mathbf{n}_1 = \mathbf{n}$, then rotating $\mathbf{c}_1$ into **c** to produce unit vectors $(\hat{\lambda}_R)_1$ and $(\hat{\theta}_R)_1$ in the tangential Cartesian plane. Thus

$$h_\lambda(\hat{\lambda}_R)_1 + h_\theta(\hat{\theta}_R)_1$$

has the same magnitude as $\mathbf{h}_1$ and its direction is the projection of $\mathbf{h}_1$ in the $(\hat{\lambda}^0, \hat{\theta}^0)$ plane. Finally **c** and **n** are expressed in terms of $\hat{\lambda}^0$ and $\hat{\theta}^0$ in order to find the required components of $\mathbf{h}_1$ in the tangential Cartesian plane.

Thus a semi-Lagrangian semi-implicit time discretization of the horizontal momentum equation (28) in tangential Cartesian coordinates gives

$$\left\{\left(\frac{u}{a} + \frac{\Delta t}{a^2 \cos\theta}\frac{\partial \Phi}{\partial \lambda}\right)\hat{\lambda}_R + \left(\frac{v}{a} + \frac{\Delta t}{a^2}\frac{\partial \Phi}{\partial \theta}\right)\hat{\theta}_R\right\}^+ = (p_\lambda \hat{\lambda}_R + p_\theta \hat{\theta}_R)^- - 2\Delta t(r_\lambda \hat{\lambda} + r_\theta \hat{\theta})^0 \quad (32)$$

where

$$p_\lambda = P_1/\cos\theta \quad (33)$$

$$p_\theta = P_2/\cos\theta \quad (34)$$

$$(r_\lambda)^0 = \left\{\frac{A(U, V, U)}{\cos\theta} - f\frac{v}{a}\right\}^0 - \frac{u^*}{a}\left(\frac{1}{\cos^2\theta}\frac{\partial U}{\partial \lambda} - \frac{v}{a}\tan\theta\right)^0 - \frac{v^*}{a}\left(\frac{1}{\cos\theta}\frac{\partial U}{\partial \theta} + \frac{u}{a}\tan\theta\right)^0 \quad (35)$$

$$(r_\theta)^0 = \left\{\frac{A(U, V, V)}{\cos\theta} + \frac{u^2 + v^2}{a^2}\tan\theta + f\frac{u}{a}\right\}^0 - \frac{u^*}{a} \times \left(\frac{1}{\cos^2\theta}\frac{\partial V}{\partial \lambda} + \frac{u}{a}\tan\theta\right)^0 - \frac{v^*}{a}\left(\frac{1}{\cos\theta}\frac{\partial V}{\partial \theta} + \frac{v}{a}\tan\theta\right)^0 \quad (36)$$

with P_1 and P_2 as given by (19) and (20), respectively. In (35) and (36) use has been made of

$$(\mathbf{v}'_H \cdot \nabla_H)\mathbf{A}_H = \left(\mathbf{v}'_H \cdot \nabla_H A_\lambda - \frac{u'}{a}A_\theta \tan\theta\right)\hat{\lambda} + \left(\mathbf{v}'_H \cdot \nabla_H A_\theta + \frac{u'}{a}A_\lambda \tan\theta\right)\hat{\theta}$$

which is valid in spherical polar coordinates for horizontal advection of an arbitrary horizontal vector

$$\mathbf{A}_H = A_\lambda \hat{\lambda} + A_\theta \hat{\theta}$$

by an arbitrary advecting horizontal velocity

$$\mathbf{v}'_H = u'\hat{\lambda} + v'\hat{\theta}.$$

The details of the transformation to the tangential Cartesian plane are presented in the Appendix where equations (A14)–(A18) give

$$\hat{\lambda}_R{}^\pm = \frac{Y^\pm \hat{\lambda}^0 + X^\pm \hat{\theta}^0}{\cos\theta^\pm} \quad (37)$$

$$\hat{\theta}_R{}^\pm = \frac{Y^\pm \hat{\theta}^0 - X^\pm \hat{\lambda}^0}{\cos\theta^\pm} \quad (38)$$

where

$$\cos\theta^\pm = (X^2 + Y^2)^\pm \quad (39)$$

$$X^\pm = \sin\alpha^\pm \cos\gamma \sin\theta^0 + (1 - \cos\alpha^\pm)\sin\gamma \cos\gamma \cos\theta^0 \quad (40)$$

$$Y^\pm = \cos\theta^0 - \sin\alpha^\pm \sin\gamma \sin\theta^0 - (1 - \cos\alpha^\pm)\sin^2\gamma \cos\theta^0 \quad (41)$$

with γ being the angle between **c** and $\hat{\lambda}^0$. Substituting

(37)–(39) into (32) and picking off the components of $\hat{\lambda}^0$ and $\hat{\theta}^0$ leads to

$$\left(U + \frac{\Delta t}{a^2}\frac{\partial \Phi}{\partial \lambda}\right)^+ = X^+ q_2 + Y^+ q_1 \qquad (42)$$

$$\left(V + \frac{\Delta t}{a^2}\cos\theta \frac{\partial \Phi}{\partial \theta}\right)^+ = Y^+ q_2 - X^+ q_1 \qquad (43)$$

where

$$q_1 = \left(\frac{Yp_\lambda - Xp_\theta}{\sqrt{X^2 + Y^2}}\right)^- - 2\Delta t(r_\lambda)^0 \qquad (44)$$

$$q_2 = \left(\frac{Xp_\lambda + Yp_\theta}{\sqrt{X^2 + Y^2}}\right)^- - 2\Delta t(r_\theta)^0. \qquad (45)$$

The system of equations (42), (43) and (30) is solved for $U(\lambda, \theta, t + \Delta t)$, $V(\lambda, \theta, t + \Delta t)$ and $\Phi(\lambda, \theta, t + \Delta t)$ by using spectral operators in exactly the same way as for the corresponding system of equations (16)–(18) for the Eulerian spectral model.

For an Eulerian model formulation, all of the advecting velocity is treated in an Eulerian fashion, so $\mathbf{v}_H^* = \mathbf{0}$, $\mathbf{v}'_H = \mathbf{v}_H$, $\alpha^\pm = 0$ and Eqs. (30)–(45) reduce to the previous formulation given by (16)–(24).

For an interpolating semi-Lagrangian model formulation, all of the advecting velocity is treated via the semi-Lagrangian approach, so $\mathbf{v}_H^* = \mathbf{v}_H$, $\mathbf{v}'_H = \mathbf{0}$ and (35), (36) and (31) take the simple form $-fv/a$, fu/a and ΦD, respectively. The upstream positions, denoted by $\mathbf{r}(t)$ at time t and $\mathbf{r}(t - \Delta t)$ at time $t - \Delta t$, generally lie between Gaussian grid points, which requires the use of interpolation in order to evaluate the fields at $(\ )^0$ and $(\ )^-$. The algorithms for finding $\mathbf{r}(t)$, $\mathbf{r}(t - \Delta t)$, and for interpolating are as described by Ritchie (1987). Two iterations are used in finding $\mathbf{r}(t)$ in this centered scheme. After $\mathbf{r}(t)$ and $\mathbf{r}(t - \Delta t)$ have been found, bicubic interpolation on the Gaussian grid is used to evaluate the fields at $(\ )^0$ and $(\ )^-$.

For a noninterpolating semi-Lagrangian model formulation, $\mathbf{v}_H^*$ is chosen to be the velocity that gives advection from the Gaussian grid point $\mathbf{r}^*(t - \Delta t)$ nearest the upstream location $\mathbf{r}(t - \Delta t)$, thus eliminating the need for interpolation at time $t - \Delta t$. The $\mathbf{v}'_H$ is the residual velocity and $(\ )^0$ denotes evaluation at time t at the midpoint of the trajectory between $\mathbf{g}$ and $\mathbf{r}^*(t - \Delta t)$. The algorithms for finding these positions are also as presented by Ritchie (1987). In general, the midpoint of the trajectory will not be a Gaussian grid point, so that interpolation is required to evaluate the fields at $(\ )^0$. The formulations of r_λ, r_θ and r_3 are as given by (35), (36) and (31) respectively, where the advection terms are calculated using the same spectral operators as in the Eulerian model.

4. Model intercomparison experiments

In order to test the application of the semi-Lagrangian method to a spectral model of the shallow water equations, an intercomparison test was performed in which four models were run to produce five-day forecasts. The models started from a FGGE analysis valid at 0000 UTC 21 December 1978 for which the initialized (via a normal mode initialization) 500 mb geopotential field for the Northern Hemisphere is shown in Fig. 2. The models were global and used no filters. In order to start, the centered time scheme requires field values at times $t = 0$ and $t = \Delta t$. The values at $t = \Delta t$ were provided by a slow start procedure which uses a forward step to produce values at $t = \Delta t/2$, followed by a centered step to give the required values at $t = \Delta t$.

The first comparison was between the two Eulerian formulations presented in section 2 where it was claimed that there is an algebraic equivalence between the conventional ζ–D formulation and the U–V formulation introduced to facilitate implementation of the semi-Lagrangian method. The model results showed that the global area-weighted root-mean-square (rms) differences between the 500 mb geopotential height forecasts produced by the two models were zero to machine accuracy out to five days, indicating that the U–V Eulerian model is indeed simply a reorganization of the calculations performed in the ζ–D one.

Having thus validated the U–V Eulerian model, a test was done to assess the impact of introducing the semi-Lagrangian treatments presented in section 3. The three U–V formulations (Eulerian, interpolating semi-Lagrangian, and noninterpolating semi-Lagrangian) were run using a triangular 126-wave (T126) truncation. The Eulerian model was run with a time step of 10 min, which respects the CFL limit, while the semi-Lagrangian models used a time step of one hour. An integration of the Eulerian model with a triangular 213-wave (T213) truncation and a time step of 6 min was

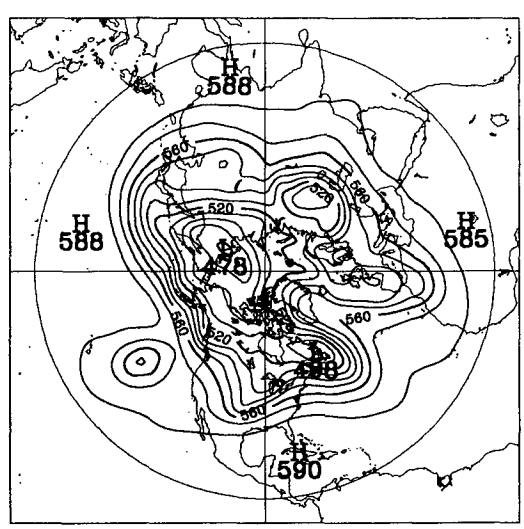

FIG. 2. Initialized 500 mb geopotential height for Northern Hemisphere 0000 UTC 21 December 1978. Contour interval 10 dam.

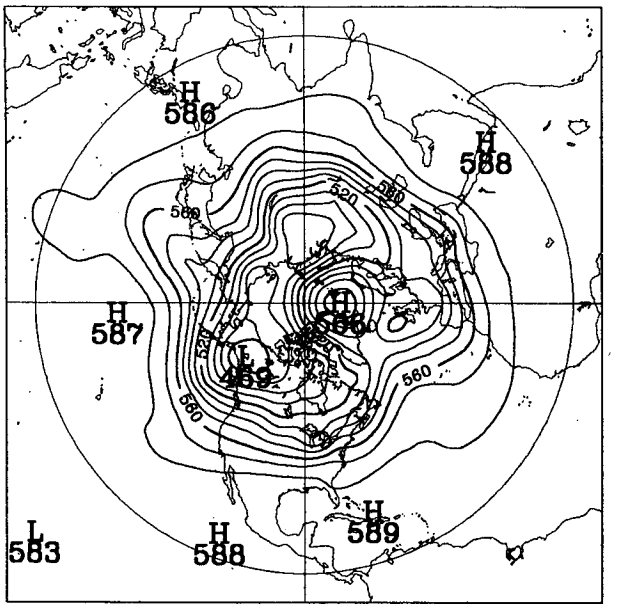

FIG. 3. T213 Eulerian control model 120 h forecast of 500 mb geopotential height for Northern Hemisphere. Contour interval 10 dam.

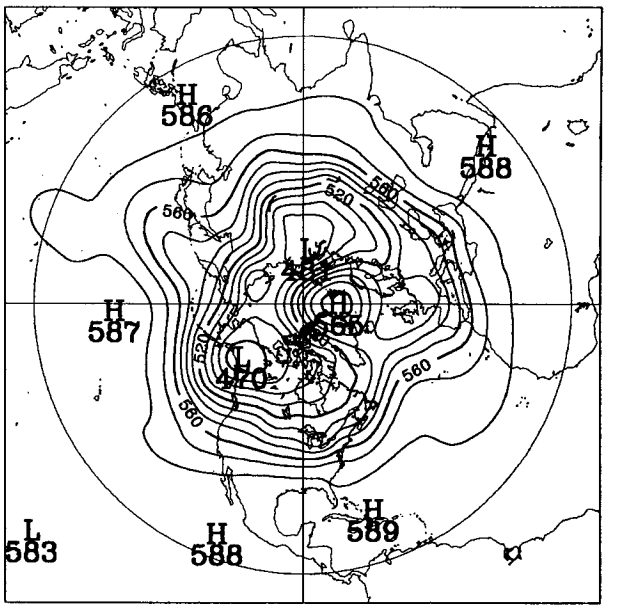

FIG. 5. As in Fig. 4 except for interpolating semi-Lagrangian model with 60 min time step.

used as a control run for the experiment. The 120 h forecast produced by the control run is shown in Fig. 3. As can be seen by comparing Figs. 2 and 3, the most notable developments during the period are the intense ridge that pushes northward across Greenland to develop into a 566 dam high, and the low pressure system that moves eastward and deepens by 120 h to a central height of 469 dam over the Yukon.

The corresponding 120 h forecasts produced by the T126 Eulerian, interpolating semi-Lagrangian, and noninterpolating semi-Lagrangian models are shown in Figs. 4, 5 and 6. A comparison among Figs. 3 to 6 shows good agreement on the positions and intensities of all the height centers. In Fig. 4 the low over the

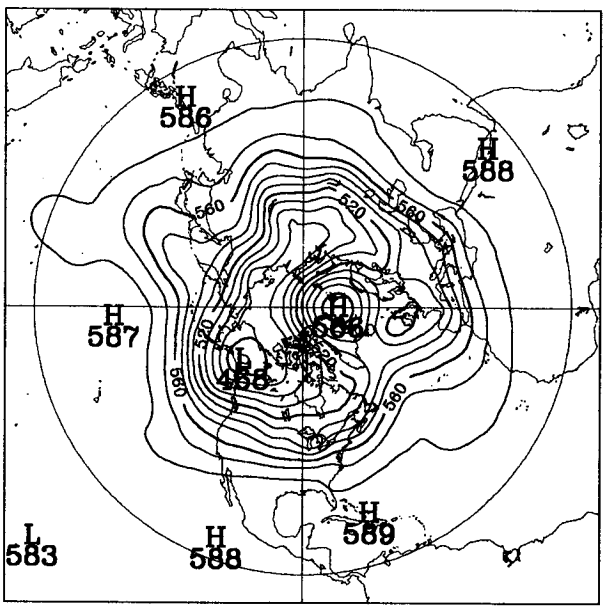

FIG. 4. T126 Eulerian model 120 h forecast of 500 mb geopotential height for Northern Hemisphere. Time step 10 min. Contour interval 10 dam.

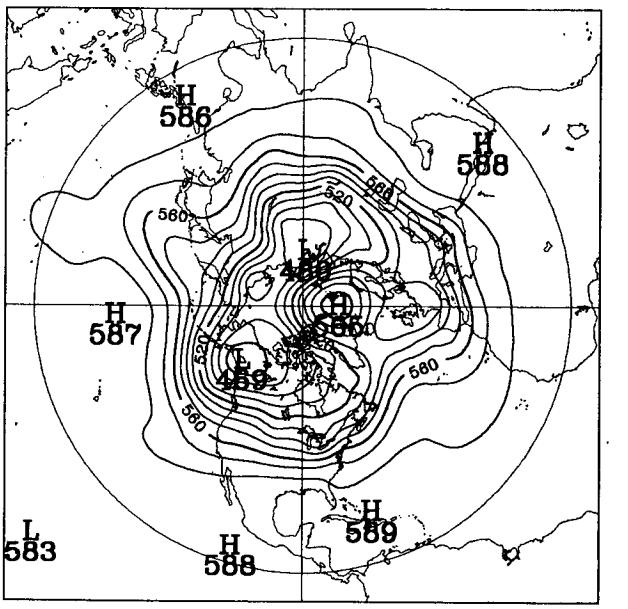

FIG. 6. As in Fig. 4 except for noninterpolating semi-Lagrangian model with 60 min time step.

Yukon is slightly deeper than in the control run, but there is very good agreement for the high near Greenland. The interpolating semi-Lagrangian model forecast is slightly less intense for both of these features, perhaps showing an impact of the damping caused by the interpolation, but the differences are very small. The noninterpolating semi-Lagrangian scheme, on the other hand, shows good agreement with the control run for the low over the Yukon, but the high near Greenland is slightly weaker.

For a more quantitative intercomparison, the global area-weighted rms differences among the forecasts of the 500 mb geopotential height were calculated after each 24 hour interval. In Fig. 7 each T126 model is compared to the control run, with the results for the Eulerian model being given by the solid curve, while the long dashed curve presents the interpolating semi-Lagrangian model results, and the short dashed curve gives the noninterpolating semi-Lagrangian ones. These results are expressed in meters and show that the semi-Lagrangian models both give an accuracy that is quite acceptable in comparison with the Eulerian model at the same resolution. The rms difference between any one of these models and the control run is small in comparison with the 500 mb geopotential height errors for typical model forecasts (for example, see Fig. 1 of Arpe et al. 1985, or Fig. 14 of Simmons 1986).

It is also interesting to compare the T126 models amongst themselves, rather than against the T213 control run. This is done in Fig. 8, where the solid curve compares the interpolating semi-Lagrangian model to the Eulerian one, the long dashed curve compares the noninterpolating semi-Lagrangian model to the Eulerian one, and the short dashed curve presents the difference between the two semi-Lagrangian models.

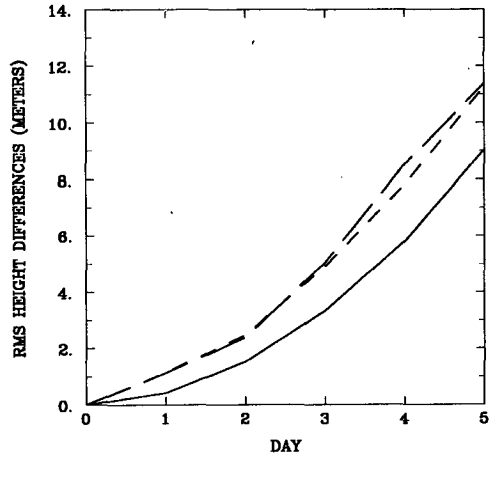

FIG. 7. Global rms differences between T126 and control run forecasts of 500 mb geopotential height in meters. Curves are plotted for Eulerian model with 10 min time step (solid), interpolating semi-Lagrangian model with 60 min time step (long dashed), and noninterpolating semi-Lagrangian model with 60 min time step (short dashed) as discussed in text.

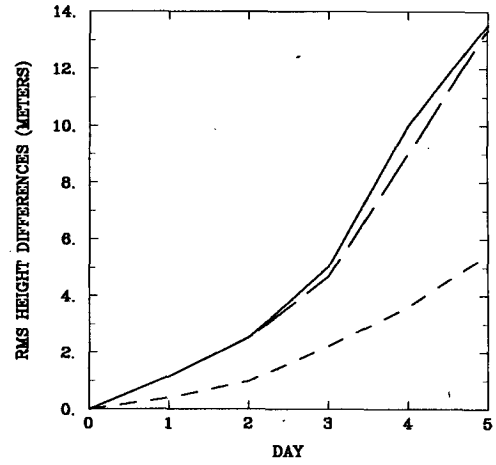

FIG. 8. Global rms differences between T126 model forecasts of 500 mb geopotential height in meters. Time steps are 10 min for the Eulerian model and 60 min for the semi-Lagrangian models. Curves are plotted for interpolating semi-Lagrangian vs Eulerian (solid), noninterpolating semi-Lagrangian vs Eulerian (long dashed) and interpolating vs noninterpolating semi-Lagrangian (short dashed) as discussed in text.

From these results it is seen that the semi-Lagrangian models are closer to each other than either is to the Eulerian. Similar results were presented by Ritchie (1986) for grid point models of the shallow water equations.

In looking at the vorticity and divergence fields, it was found that they were becoming somewhat noisy by the end of the integrations of these unfiltered Eulerian and noninterpolating semi-Lagrangian models. No such noise appeared in the interpolating semi-Lagrangian model fields, probably because of the smoothing due to the damping inherent in the interpolation. This is suggested by considering the enstrophy spectra at 120 h as displayed in Fig. 9. The enstrophy is given by

$$\frac{\overline{\zeta^2}}{2} = \sum_n E_n$$

where the overbar is the area weighted average and E_n is the enstrophy associated with two-dimensional wavenumber n. In producing the values presented in Fig. 9, the values of E_n have been summed in groups of five consecutive values of n (n = 1–5, 6–10, 11–15, · · ·), expressed as a percentage of the total initial enstrophy in the run, and plotted as a function of the central wavenumber (3, 8, 13, . . .) in each group. The results are given by the long dashed curve for the T126 Eulerian model (corresponding to Fig. 4), the short dashed curve for the T126 noninterpolating semi-Lagrangian model (corresponding to Fig. 6), the variable dashed curve for the interpolating semi-Lagrangian model (corresponding to Fig. 5), and the solid curve for the T213 Eulerian control model (corresponding

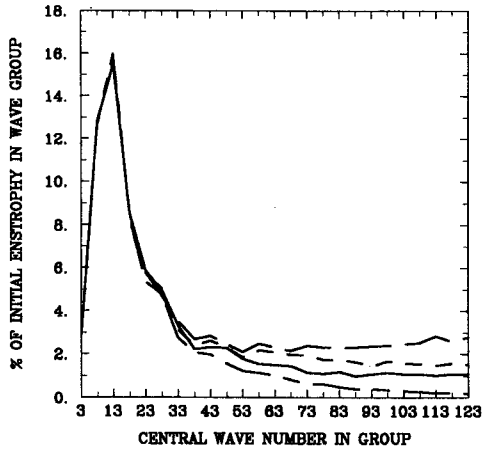

FIG. 9. Enstrophy spectra at 120 h. Results are expressed as a percentage of the total initial enstrophy in the run and plotted as a function of the central wavenumber in groups of five consecutive two-dimensional wave numbers (see text). Curves are plotted for the T126 Eulerian model (long dashed), the T126 noninterpolating semi-Lagrangian model (short dashed), the T126 interpolating semi-Lagrangian model (variable dashed), and the T213 Eulerian control model (solid).

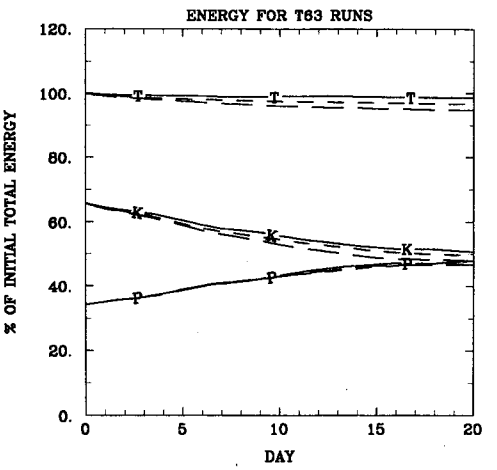

FIG. 10. Evolution of potential (P), kinetic (K), and total (T) energy in 20 day T63 integrations as discussed in text. Solid curves are for the noninterpolating semi-Lagrangian model, and long dashed curves are for the interpolating one. Short dashed curves give evolution for T106 Eulerian model with diffusion and are included to indicate behavior in typical medium range forecasts. Energies are expressed as a percentage of the initial total energy for the run.

to Fig. 3). In comparison with the T213 control run, it is seen that the T126 Eulerian model is noisy in the sense that too much enstrophy has accumulated in the short scales (large wavenumbers) in the model. In the noninterpolating semi-Lagrangian model, this "spectral blocking" behavior is also present, but to a lesser extent. For the interpolating semi-Lagrangian model, on the other hand, the short scales have less enstrophy than in the control run.

Another point of some interest is the energy conservation properties of these schemes for longer integrations. In order to examine this question, the interpolating and noninterpolating semi-Lagrangian models were run out to 20 days with a 60 min time step at resolutions of T63 (triangular 63-wave truncation) and T126. The interpolating model had no filters, while the noninterpolating one had a Robert time filter with a weak coefficient of $\nu = 0.04$ at T63 and $\nu = 0.02$ at T126 (using the definition of ν as given in the analysis by Asselin 1972). We define the potential energy per unit mass as

$$P = \frac{\overline{(\Phi_D{}^2)}}{2\overline{\Phi_T}}$$

and the kinetic energy per unit mass as

$$K = \frac{a^2}{\overline{\Phi_T}}\left\{\frac{\overline{\Phi_T(U^2 + V^2)}}{2\cos^2\theta}\right\}$$

where

$$\Phi_T = \Phi^* + \Phi$$

$$\Phi_D = \Phi_T - \overline{\Phi_T}.$$

The evolutions of P, K, and the total energy $T = P + K$ are presented in Fig. 10 for the T63 runs and Fig. 11 for the T126 runs. The energies for each run are expressed as a percentage of the initial total energy for the run. Here the solid curves are for the noninterpolating model and the long dashed curves are for the interpolating one. As an indication of the energy conservation behavior that is considered to be acceptable in typical medium range forecasts (e.g., see Jarraud et al. 1985), the Eulerian model was run at a resolution of T106 (triangular 106-wave truncation) with a time step of 12 min, and a ∇^4 diffusion with a coefficient of 10^{15} m^4 s^{-1} was applied to the vorticity, divergence, and perturbation geopotential. The evolutions of P, K and T for this model are given by the short dashed

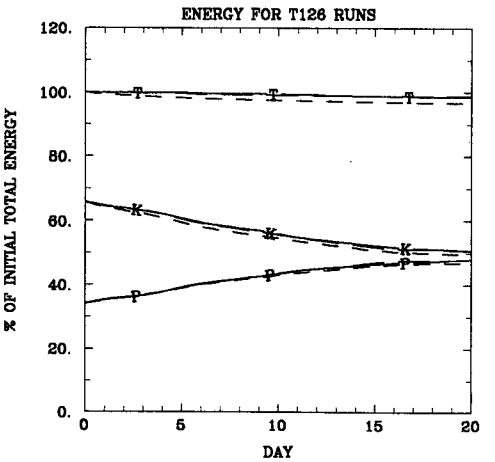

FIG. 11. As in Fig. 10 except for T126 integrations.

curves in Figs. 10 and 11. At all resolutions, all models have very similar evolutions of potential energy and the models appear to be evolving towards a state of equipartition of kinetic and potential energy. For the T106 Eulerian run, the loss in total energy after 20 days is about 3%. At the lower resolution (T63, Fig. 10) the decay of kinetic energy for the interpolating model is a little excessive, resulting in a loss of about 5% in total energy, while the noninterpolating model conserves total energy to within about 1%. At the higher resolution (T126, Fig. 11), the effect of damping in the interpolating scheme is much smaller and both semi-Lagrangian models conserve total energy to within about 1%. Note that the two semi-Lagrangian models are almost indistinguishable (the solid and long dashed curves almost superimpose) in this figure, and both give better energy conservation than the T106 Eulerian model (short dashed curves). All these runs have very good mass conservation characteristics, conserving mean perturbation geopotential to within half a percent.

Overall, these results demonstrate that both interpolating and noninterpolating semi-Lagrangian schemes can be applied accurately and stably to spectral models of the shallow-water equations using time steps that far exceed the CFL limit for the corresponding Eulerian model.

5. Discussion

This paper has examined the application of the semi-Lagrangian method to a spectral model of the shallow water equations. As a point of departure for the study, a conventional ζ–D Eulerian formulation was presented in section 2, where an algebraically equivalent U–V Eulerian formulation was also developed to facilitate the introduction of the semi-Lagrangian method. Interpolating and noninterpolating semi-Lagrangian model formulations were presented in section 3. In order to avoid an instability associated with an explicit treatment of the metric term in semi-Lagrangian models in spherical polar coordinates, the vector form of the horizontal momentum equation was treated with a semi-implicit semi-Lagrangian discretization and was integrated in a tangential Cartesian coordinate system. A detailed study of this instability and the integration in a tangential Cartesian coordinate system will be the subject of a forthcoming paper. In an independent study, Bates (1988) has integrated the vector form of the horizontal momentum equation in applying the semi-Lagrangian scheme to a grid point model of the shallow water equations on the sphere. The model intercomparison experiments in section 4 confirm the equivalence of the Eulerian models formulated in section 2, and assess the impact of introducing the semi-Lagrangian treatments presented in section 3. The results show that both interpolating and noninterpolating semi-Lagrangian schemes can be applied accurately and stably to a spectral model of the shallow water equations using time steps that are much larger than the CFL limit for the corresponding Eulerian model.

It is worth noting that all the models presented here use the same algorithms to solve spectrally the semi-implicit system of equations (7), (8) and (10) for the ζ–D model, or (25)–(27) for the U–V models. The differences in model formulations deal mostly with operations on the Gaussian grid that are necessary to calculate the right-hand side of these equations, which facilitates the conversion from the Eulerian ζ–D model to the semi-Lagrangian U–V models.

In the grid-point model investigation of the noninterpolating semi-Lagrangian scheme (Ritchie 1986), the residual advection terms were treated with second-order space differencing. By using a spectral calculation of the derivatives, this present study significantly increases the accuracy of the calculations and produces an improvement in the overall precision.

Although the algorithms for calculating trajectories and interpolating are identical to those used in the problem of simple advection by a steady wind (Ritchie 1987), the shallow water equations provide a much more demanding and realistic test of the suitability of these methods for spectral models that are used in numerical weather prediction. The next logical extension is an application to a three-dimensional primitive equations spectral model.

For the T126 runs in section 4, the semi-Lagrangian models use a time step Δt that is six times as large as the one used in the Eulerian model. Due to the overhead of the additional operations required by the semi-Lagrangian schemes at each time step, the overall improvement in efficiency is less than a factor of 6. These additional operations do vectorize fully on the CRAY X-MP, but the models have not been fully optimized yet. Consequently, specific timings may be premature at this stage. Nevertheless, execution times for the T126 runs indicate that the semi-Lagrangian models are roughly a factor of 4 faster than the Eulerian one. In the semi-Lagrangian models, the transformations to the tangential Cartesian plane are performed throughout the whole globe and account for about 5% of the model execution time. These results indicate that the application of the semi-Lagrangian method to this spectral model of the shallow water equations is already giving efficiency improvements comparable to those being reported for grid point models.

Acknowledgments. The author wishes to thank his colleagues at Recherche en prévision numérique for many helpful discussions during the course of this work. He is especially indebted to André Robert for identifying the instability problem mentioned at the beginning of section 3 and for recommending the integration in tangential Cartesian coordinates as implemented here. Clive Temperton implemented the nor-

mal mode initialization procedure for these tests, and Jean Côté provided the T213 Eulerian integration used as a control run in section 4. Thanks are also expressed to Diane Lespérance for typing the manuscript and to Jean Côté for reviewing it.

APPENDIX

Transforming Horizontal Vectors to the Tangential Cartesian Plane

In order to implement the semi-Lagrangian treatment as presented in section 3, we want to transform horizontal vectors on a trajectory from their spherical polar representation to their form on the Cartesian plane tangent to the trajectory at position **R**.

As a first step, for another position $\mathbf{R}_1$ on the same trajectory, we want to describe its unit vectors $(\hat{\lambda}_1, \hat{\theta}_1)$ in terms of its coordinates (λ_1, θ_1) and the velocity $\mathbf{v}_H^*$ and coordinates (λ, θ) at position **R**. As described in section 3, **c** is a unit vector along $\mathbf{v}_H^*$ and **n** is a horizontal unit vector normal and to the left of **c**, so that

$$\mathbf{c} = \cos\gamma\hat{\lambda} + \sin\gamma\hat{\theta} \tag{A1}$$

$$\mathbf{n} = -\sin\gamma\hat{\lambda} + \cos\gamma\hat{\theta} \tag{A2}$$

and

$$\mathbf{v}_H^* = \{(u^*)^2 + (v^*)^2\}^{1/2}\mathbf{c}$$

where

$$\gamma = \tan^{-1}v^*/u^*$$

(see Fig. 12). Let α be the angular displacement along the great circle trajectory from **R** to $\mathbf{R}_1$. Assuming motion with constant speed along the trajectory gives

$$\alpha = \{(u^*)^2 + (v^*)^2\}^{1/2}\Delta t/a.$$

From Fig. 1 it is seen that

$$\mathbf{R}_1 = \cos\alpha\mathbf{R} + a\sin\alpha\mathbf{c}.$$

Incorporating (A1) leads to

$$\mathbf{R}_1 = \cos\alpha\mathbf{R} + a\sin\alpha(\cos\gamma\hat{\lambda} + \sin\gamma\hat{\theta}). \tag{A3}$$

This is solved for the relationship between coordinates (λ_1, θ_1) at position $\mathbf{R}_1$ and the velocity (i.e., α and γ) and coordinates (λ, θ) at position **R** by introducing a Cartesian coordinate system whose origin is at the center of the sphere and whose basis vectors are (**I**, **J**, **K**), a right-handed triad at this origin. The transformation from spherical polar $(\hat{\lambda}, \hat{\theta}, \mathbf{k})$ coordinates to these Cartesian coordinates is given by

$$\hat{\lambda} = -\sin\lambda\mathbf{I} + \cos\lambda\mathbf{J} \tag{A4}$$

$$\hat{\theta} = -\cos\lambda\sin\theta\mathbf{I} - \sin\lambda\sin\theta\mathbf{J} + \cos\theta\mathbf{K} \tag{A5}$$

$$\mathbf{k} = \cos\lambda\cos\theta\mathbf{I} + \sin\lambda\cos\theta\mathbf{J} + \sin\theta\mathbf{K}. \tag{A6}$$

Resolving (A3) into Cartesian components yields

$$\cos\lambda_1\cos\theta_1 = \cos\lambda\cos\theta\cos\alpha - \sin\alpha(\sin\lambda\cos\gamma + \cos\lambda\sin\theta\sin\gamma)$$

$$\sin\lambda_1\cos\theta_1 = \sin\lambda\cos\theta\cos\alpha + \sin\alpha(\cos\lambda\cos\gamma - \sin\lambda\sin\theta\sin\gamma)$$

$$\sin\theta_1 = \sin\theta\cos\alpha + \cos\theta\sin\alpha\sin\gamma. \tag{A7}$$

With a little further manipulation, the first two of these equations lead to

$$\cos(\lambda_1 - \lambda)\cos\theta_1 = \cos\theta\cos\alpha - \sin\theta\sin\alpha\sin\gamma \tag{A8}$$

$$\sin(\lambda_1 - \lambda)\cos\theta_1 = \sin\alpha\cos\gamma. \tag{A9}$$

Using (**c**, **n**, **k**) as basis vectors, $\hat{\lambda}_1$ and $\hat{\theta}_1$ can be written as

$$\hat{\lambda}_1 = (\hat{\lambda}_1\cdot\mathbf{c})\mathbf{c} + (\hat{\lambda}_1\cdot\mathbf{n})\mathbf{n} + (\hat{\lambda}_1\cdot\mathbf{k})\mathbf{k}$$

$$\hat{\theta}_1 = (\hat{\theta}_1\cdot\mathbf{c})\mathbf{c} + (\hat{\theta}_1\cdot\mathbf{n})\mathbf{n} + (\hat{\theta}_1\cdot\mathbf{k})\mathbf{k}.$$

Expanding **c** and **n** in the dot products using (A1) and (A2), evaluating the resulting expressions in Cartesian coordinates with the help of (A4)–(A6), and simplifying via (A7)–(A9) leads to

$$\cos\theta_1\hat{\lambda}_1 = \cos\theta\cos\gamma(\cos\alpha\mathbf{c} - \sin\alpha\mathbf{k}) + (\sin\theta\sin\alpha - \cos\theta\cos\alpha\sin\gamma)\mathbf{n} \tag{A10}$$

$$\cos\theta_1\hat{\theta}_1 = -(\sin\theta\sin\alpha - \cos\theta\cos\alpha\sin\gamma) \times (\cos\alpha\mathbf{c} - \sin\alpha\mathbf{k}) + \cos\theta\cos\gamma\mathbf{n}. \tag{A11}$$

It is seen from Fig. 1 that

$$\mathbf{c}_1 = \cos\alpha\mathbf{c} - \sin\alpha\mathbf{k}$$

and substituting this in (A10)–(A11) gives:

$$\cos\theta_1\hat{\lambda}_1 = \cos\theta\cos\gamma\mathbf{c}_1 + (\sin\theta\sin\alpha - \cos\theta\cos\alpha\sin\gamma)\mathbf{n} \tag{A12}$$

$$\cos\theta_1\hat{\theta}_1 = -(\sin\theta\sin\alpha - \cos\theta\cos\alpha\sin\gamma)\mathbf{c}_1 + \cos\theta\cos\gamma\mathbf{n}. \tag{A13}$$

As outlined in section 3, the next step is to rotate $\mathbf{c}_1$ into **c** in order to produce unit vectors $(\hat{\lambda}_R)_1$ and $(\hat{\theta}_R)_1$ in the plane tangent to the trajectory at position **R**. To do this, simply replace $\mathbf{c}_1$ by **c**, $\hat{\lambda}_1$ by $(\hat{\lambda}_R)_1$, and $\hat{\theta}_1$ by $(\hat{\theta}_R)_1$ in (A12) and (A13). Finally **c** and **n** are

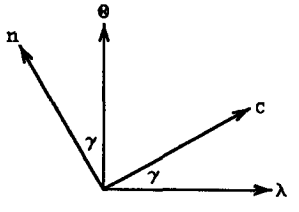

FIG. 12. Schematic diagram showing relationships among horizontal unit vectors at position **R** as used in transforming horizontal vectors to the tangential Cartesian plane.

expressed in terms of $\hat{\lambda}$ and $\hat{\theta}$ by using (A1) and (A2). This leads to the following results which are used in section 3:

$$(\hat{\lambda}_R)_1 = \frac{Y_1\hat{\lambda} + X_1\hat{\theta}}{\cos\theta_1} \tag{A14}$$

$$(\hat{\theta}_R)_1 = \frac{Y_1\hat{\lambda} - X_1\hat{\theta}}{\cos\theta_1} \tag{A15}$$

where

$$\cos\theta_1 = \{(X_1)^2 + (Y_1)^2\}^{1/2} \tag{A16}$$

$$X_1 = \sin\alpha\cos\gamma\sin\theta + (1 - \cos\alpha)\sin\gamma\cos\gamma\cos\theta \tag{A17}$$

$$Y_1 = \cos\theta - \sin\alpha\sin\gamma\sin\theta - (1 - \cos\alpha)\sin^2\gamma\cos\theta. \tag{A18}$$

REFERENCES

Arpe, K., A. Hollingsworth, M. S. Tracton, A. C. Lorenc, S. Uppala and P. Kållberg, 1985: The response of numerical weather prediction systems to FGGE level IIb data. Part II: Forecast verifications and implications for predictability. *Quart. J. Roy. Meteor. Soc.*, **111,** 67–101.

Asselin, R., 1972: Frequency filter for time integrations. *Mon. Wea. Rev.*, **100,** 487–490.

Bates, J. R., and A. McDonald, 1982: Multiply-upstream, semi-Lagrangian advective schemes: Analysis and application to a multilevel primitive equation model. *Mon. Wea. Rev.*, **110,** 1831–1842.

——, 1988: Finite-difference semi-Lagrangian techniques for integrating the shallow water equations on the sphere. *ECMWF Workshop on Techniques for the Horizontal Discretization in NWP Models.* European Centre for Medium Range Weather Forecasts, Shinfield Park, Reading, Berkshire RG2 9AX, England (to be published).

Bourke, W., 1972: An efficient, one-level, primitive equation spectral model. *Mon. Wea. Rev.*, **100,** 683–689.

Daley, R., C. Girard, J. Henderson and I. Simmonds, 1976: Short term forecasting with a multi-level spectral primitive equations model. *Atmosphere,* **14,** 98–134.

Eliasen, E., B. Machenhauer and E. Rasmussen, 1970: On a numerical method for integration of the hydrodynamical equations with a spectral representation of the horizontal fields. Rep. No. 2, Institute of Theoretical Meteorology, University of Copenhagen, Haraldsgade 5, DK-2200 Copenhagen N, Denmark, 35 pp.

Jarraud, M., A. J. Simmons and M. Kanamitsu, 1985: Development of the high resolution model. Tech. Memo. No. 107, Research Department, European Centre for Medium Range Weather Forecasts, Shinfield Park, Reading, Berkshire RG2 9AX, England.

McDonald, A., 1986: A semi-Lagrangian and semi-implicit two time level integration scheme. *Mon. Wea. Rev.*, **114,** 824–830.

Machenhauer, B., 1979: The spectral method. *Numerical Methods in Atmospheric Models,* Vol. II, Garp Publ. Ser. No. 17, 499 pp.

Ritchie, H., 1985: Application of a semi-Lagrangian integration scheme to the moisture equation in a regional forecast model. *Mon. Wea. Rev.*, **113,** 424–435.

——, 1986: Eliminating the interpolation associated with the semi-Lagrangian scheme. *Mon. Wea. Rev.*, **114,** 135–146.

——, 1987: Semi-Lagrangian advection on a Gaussian grid. *Mon. Wea. Rev.*, **115,** 608–619.

Robert, A., 1966: The integration of a low order spectral form of the primitive meteorological equations. *J. Meteor. Soc. Japan,* **44,** 237–244.

——, 1981: A stable numerical integration scheme for the primitive meteorological equations. *Atmos. Ocean,* **19,** 35–46.

——, 1982: A semi-Lagrangian and semi-implicit numerical integration scheme for the primitive meteorological equations. *J. Meteor. Soc. Japan,* **60,** 319–325.

——, T. L. Yee and H. Ritchie, 1985: A semi-Lagrangian and semi-implicit numerical integration scheme for multilevel atmospheric models. *Mon. Wea. Rev.*, **113,** 388–394.

Sawyer, J. S., 1963: A semi-Lagrangian method of solving the vorticity advection equation. *Tellus,* **15,** 336–342.

Simmons, A. J., 1986: Numerical prediction: Some results from operational forecasting at ECMWF. pp. 305–338 of *Advances in Geophysics,* Vol. 29, Academic Press, 459 pp.

Staniforth, A., and C. Temperton, 1986: Semi-implicit semi-Lagrangian integration schemes for a barotropic finite-element regional model. *Mon. Wea. Rev.*, **114,** 2078–2090.

Temperton, C., and A. Staniforth, 1987: An efficient two-time-level semi-Lagrangian semi-implicit integration scheme. *Quart. J. Roy. Meteor. Soc.*, **113,** 1025–1039.